Remote Sensing detectability of airborne Arctic dust

Norman T. O'Neill[1], Keyvan Ranjbar[2], Liviu Ivănescu[3], Yann Blanchard[4], Seyed Ali Sayedain[1], Yasmin AboEl-Fetouh[5]

[1]Centre d'Applications et de Recherches en Télédétection, Université de Sherbrooke, Sherbrooke, Canada
5 [2]Flight Research Laboratory, National Research Council Canada, Ottawa, Canada
[3]Metrology Research Centre, National Research Council Canada, Ottawa, Canada
[4]Centre pour l'Étude et la Simulation du Climat à l'Échelle Régionale, Département des sciences de la Terre et de l'atmosphère, Université du Québec à Montréal, Montréal, Canada
[5]Institute of Meteorology and Climate Research, Karlsruhe Institute of Technology, Karlsruhe, Germany

10 *Correspondence to:* N. T. O'Neill (Norman.T.ONeill@USherbrooke.ca)

Abstract. Remote sensing (RS) based estimates of Arctic dust are oftentimes overestimated due to a failure in separating out the dust contribution from that of spatially homogeneous clouds or low-altitude cloud-like plumes. A variety of illustrations are given with a particular emphasis on claims of using brightness temperature differences (BTDs) as a signature indicator of Arctic dust transported from mid-latitude deserts or generated by local Arctic sources. While there is little dispute about the

15 presence of both Asian and local dust across the Arctic, the direct RS detectability of airborne dust, as ascribed to satellite (MODIS and AVHRR) measurements of significantly negative brightness-temperature differences at 11 and 12 µm (BTD_{11-12}) has been misrepresented in certain cases. While it is difficult to account for all examples of strongly negative BTD_{11-12} values in the Arctic, it is unlikely that airborne dust plays a significant role. One, much more likely contributor would be water plumes in the Arctic inversion layer.

20 The RS detectability of the impact of Arctic dust (notably due to Arctic dust from local sources) can, however, be of significance. Sustained dust deposition can substantially decrease (visible to shortwave IR) snow and ice reflectance albedo (pan-chromatic reflectance) and the signal measured by satellite sensors. Significantly negative BTD_{11-12} values would however only represent a limited area near the drainage basin sources according to our event-level case studies. The enhanced INP (Ice Nucleating Particle) role of local Arctic dust can, for example, induce significant changes in the properties of low-level mixed-

25 phase clouds (cloud optical depth changes $<\sim 1$) that can be readily detected by active and passive RS instruments. It is critical that the distinction between the RS detectability of airborne Arctic dust versus the RS detectability of the impacts of that dust be understood if we are to appropriately parameterize, for example, the radiative forcing influence of dust in this climate sensitive region.

1 Introduction

30 Vincent (2018) (VCT) reported on the use of MODIS and AVHRR thermal infrared (TIR) brightness temperature differences (BTDs) in the western Canadian Arctic (Beaufort Sea and Amundsen Gulf region) to detect the presence of "persistent low-

level dust clouds" and dust deposited on ice, snow and water. A later publication (Bowen & Vincent, 2021) (B&V) argued that negative BTD_{11-12} ($BT_{11\,\mu m} - BT_{12\,\mu m}$) values were a unique signature of dust (without explicitly distinguishing between airborne and surface deposited dust) and could be directly used to estimate the relative spatial extent of dust in the Arctic.

35   We acknowledge the robustness of negative BTD_{11-12} values as a potential indicator of optically thick, airborne dust embedded in a normal-lapse-rate atmospheric layer or as a sign of accumulated dust deposition. We disagree with the affirmation that dust clouds of Asian origin were commonly detected using passive, satellite-based remote sensing (RS). Springtime Asian dust, while representing a robust pan-Arctic seasonal event, yields, on average, very weak coarse mode (CM) aerosol optical depths (AODs[1]). The multi-year, six-station, pan-Arctic, AERONET/AEROCAN monthly-binned (geometric means)

40   climatology of AboEl-Fetouh et al. (2020) (AeF) indicate (their Figure 7) that the Resolute Bay CM AODs are largely of the greatest amplitude across the six stations. Using that site as a reference, the CM AODs will generally be $<\sim$ the Resolute Bay value ($0.016 \times 1.5^{\pm1}$ during the Asian-dust dominated April, May springtime and $<\sim 0.0023 \times 1.2^{\pm1}$ during the June, July, August (likely local dust) summertime. DODs (Dust Optical Depths) will be $\sim$ CM AODs in the absence of any other significant CM source such as sea-salt or volcanic ash (or CM cloud in the absence of proper cloud screening).

45   Springtime Asian dust aerosols at such small CM AOD (DOD) values are difficult if not impossible to detect using passive satellite-based RS techniques at any wavelength. The BTD_{11-12} variation per unit change in DOD is $\sim$ -0.3 °K (see the caption of Figure S8 for details). The corresponding change in BTD_{11-12} for a springtime Asian dust DOD of 0.016 (the Resolute Bay maximum) would be an undetectable -0.005 °K (an amplitude that is significantly less than nominal MODIS BTD_{11-12} noise figure of 0.07 °K given in the Figure S8 caption).

50   While the monthly-averaged springtime Asian dust DODs are $<\sim 0.016$ there are springtime (mid-tropospheric) Asian dust events that do lead to more substantive DODs over the Arctic. In general these are limited to a few notable days in a given year with individual DODs being $<\sim 0.4$: see Appendix A.6 for details on the roughly week-long dust intrusion over the Mount Logan (Yukon territory of Canada) in April of 2001 (associated with DODs of $<\sim 0.3$), Stone et al. (2007) for the roughly week long, mid-tropospheric dust intrusions of April 2002 over Barrow, Alaska (DODs $<\sim 0.4$), Zhao et al. (2022) for moderate

55   DODs ($<\sim 0.1$) associated with single-day intrusions over Barrow in April of 2015, and Thulasiraman et el. (2002) for evidence that sub 0.4 DODs of the April, 2001 event were arguably a broad west coast phenomenon stretching from (at least) low-Arctic Canada to the southern United States. DODs ~ 0.4 could incite a marginally detectable BTD_{11-12} signal (-0.3 °K $\times$ 0.4 $\sim$ -0.12 °K) whose presence would be more easily identified in true-color and AOD imagery (at least over water).

VCT noted that a second dust source could have been locally generated dust storms (although dust from southern latitudes was

60   claimed to be the major source). Indeed, Meinander et al. (2022) recently reviewed the importance of high latitude dust generated from high latitude sources. However, even strong local dust plumes will likely not induce large DODs beyond the short temporal and spatial window associated with their detectable plume presence: outside this window, the monthly averaged

---

[1] Note that, unless otherwise stated, our AODs and DODs will be referenced to a wavelength of 550 nm

DOD upper limit reported by AeF make it very unlikely that DODs could be detected using passive, satellite-based RS in the thermal infrared red (TIR).

65 Empirical support for this affirmation is provided, for example, by Ranjbar et al.'s (2021) detection of a high-Arctic dust plume near its drainage-basin source: their MODIS BTD_{11-12} values (amplitude ~ 1.5 °K) are ~ the amplitude of the most extreme negative values (~ -1.0 °K) reported by VCT. However, Ranjbar's visible (532 nm) DODs were ~ 0.5 (a BTD_{11-12} to DOD sensitivity of $dBTD_{11-12}/dDOD$ ~ 1.5 / 0.5 = 3 °K per unit DOD). The AeF Resolute Bay summertime[2] CM AOD maximum ($0.0023 \times 1.2^{\pm 1}$) would, assuming approximate proportionality, produce generally undetectable BTD_{11-12} changes ($|BTD_{11-12}|$
70 $<\sim 3 \times 0.0023 = 0.007$ °K.

We also note that AeF's DOD statistics are ~ DOD computations derived from the simulated local dust ("Arctic dust") polar map (Figure 1) of Kawai et al. (2023): their "annual-mean vertically integrated mass concentrations" ("Arctic dust mass" in their color legend) yield DODs that vary from 0.0037 at Resolute Bay to 7.9×10^{-5} at the high Arctic site of Eureka, Nunavut, Canada (see Appendices A.1 and A.2). Their Resolute Bay DOD is ~ AeFs Resolute Bay summertime CM AOD of $0.0023 \times$
75 $1.2^{\pm 1}$ (from above).

Having argued that Arctic DODs are, in general, at the margins of RS detectability, we must also take issue with B&V's affirmation that: "While it is possible that a substance other than mineral dust is causing large-scale negative BTD_{11-12} signatures in the polar environment, there is nothing in the literature to support this conjecture.". We will present an alternative mechanism below involving inversion layer liquid clouds whose cloud optical depths (CODs) are sufficiently large to induce
80 significant negative BTD_{11-12} signatures.

In general, there is often a tendency in the literature to significantly overestimate DOD magnitudes of Asian dust. It is no trivial matter to decouple such relatively small DODs from very large CM CODs for clouds that are often in the neighbourhood of those dust plumes. Such clouds may indeed result from dust nucleation: see for e.g., Hildner et al. (2010) and their discussion involving a high-altitude Asian dust plume that apparently nucleates into a highly-depolarizing cloud (captured by the AHSRL
85 lidar above our PEARL [Polar Environment Atmospheric Research Lab] observatory at Eureka). In more general terms, Eck et al. (2009) noted the shortcomings in applying the AERONET (temporally-based) V2 cloud screening algorithm in the presence of spatially homogeneous clouds at Barrow, AK: spatially homogeneous (insufficiently variable) clouds such as thin cirrus are erroneously classified as dust (false-positive "dust"). More recently, Stone et al. (2014) underscored the potential for the same false-positive problem in their Barrow-based climatology of Arctic aerosols. Ranjbar et al. (2022) argued that the
90 authors of a case study involving the transport of Asian dust into the high Arctic likely confused DOD with nearby COD and thereby significantly overestimated the DOD of a thin Asian dust plume about 7 km above the PEARL observatory

Analogous problems plague polar winter data. O'Neill et al. (2016) used lidar profiles and a spectral cloud-screening approach to estimate the large (starphotometer-derived) CM AOD errors that would be associated with the application of frequently inadequate (temporally-based) cloud screening paradigms to polar winter AODs acquired at the PEARL. The authors

---

[2] More typical of average spring to-autumn-local DODs if one excludes the springtime Asian-dust dominated DODs

95 concluded that: "Spatially homogeneous clouds and low altitude ice clouds that remain after temporal cloud screening represent an inevitable systematic error in the estimation of AOD [more so for CM AOD]: the [positive bias] AOD error was estimated to vary from 78 to 210% at Eureka and from 2 to 157% at Ny-Ålesund.". In a not unrelated finding, Zamora et al. (2022) pointed out that the CALIPSO (CALIOP) classification algorithm was likely misclassifying wintertime "diamond dust" as mineral dust in their pan-Arctic analysis.

100 In terms of satellite-based estimates of DOD, B&V claimed that "average aerosol optical depth (AOD) is a proxy for dust aerosol concentration" and employed the 1998 to 2010 SeaWiFS AOD climatology of Hsu et al. (2012) to report a slight increase in AOD over the global oceans (and given their dust proxy assertion, a slight increase in DOD) in an apparent effort to support an increasing trend in their average RSED ("relative spatial extent of dust") parameter over the Arctic and Antarctic. This is yet another instance of DOD overestimation in the literature: AOD is almost universally dominated by (non-dust) fine

105 mode (roughly submicron) particles and cannot be viewed as a proxy for "dust aerosol concentration". The proxy assumption is especially questionable when claiming to report a trend involving a minor AOD species (dust) coupled with a satellite AOD product that is less accurate than the AOD generated from ground-based AERONET data (for which a DOD trend analysis would be a challenge on its own merits): the bias error (amplitude $>\sim 0.01$) between the SesWiFS AODs and AERONET AODs (Figure 2 of Hsu et al., 2012) are (for example) $>\sim$ AeFs spring and summer CM AOD geometric means for Resolute

110 Bay ($0.0051 \times 2.5^{\pm 1}$).

A more realistic DOD satellite product over the Arctic is the MIDAS (ModIs Dust AeroSol) data set (Gkikas et al., 2021). The MIDAS reanalysis system is based on MODIS AODs coupled with MDFs (mineral dust fraction; a semi-intensive parameter of DOD ÷ AOD) derived from MERRA-2 (Modern-Era Retrospective analysis for Research and Applications version 2) whose key components are the Goddard GOCART aerosol model and GEOS (Goddard Earth Observing System). The MIDAS annual

115 DOD (arithmetic) mean for the 2003 – 2017 period (for the more accurate retrievals over water around Resolute Bay) is $\sim 0.01 \pm 0.02$ (where 0.02 is a computed estimate of retrieval uncertainty rather than a standard deviation). The AeF Resolute Bay value of $0.0051 \times 3.0^{\pm 1}$ is contained with the MIDAS uncertainty envelope.

2 Optically detectable aerosol events in the Arctic

Arctic aerosol events that are detectable using visible to near-IR, passive, satellite-based RS techniques are, for the most part,

120 either FM (fine mode) smoke or FM Arctic haze (see AeF's Figure 1a for seasonal simulations of FM AOD over the Arctic and a FM vs CM speciation of Arctic aerosols). VCT's claim of a "strong dust event" associated with his Figure 5 (and his Figure 3b) imagery was (if aerosols were to be ascribed any role), associated with a FM smoke event induced by fires in Alaska and the Canadian Northwest Territories (see Figure S1a and its discussion).

Figure S1b shows that there is marginal correspondence at best between the position of the smoke plume over the Amundsen

125 Gulf (as evidenced by the pattern of the smoke on the true color image) and the patterns of negative blue colored BTD_{11-12} values over the water regions south of Bank's Island (at the southern extreme of the Canadian Arctic Archipelago). The

principle optical effect in the massive region of blue-colored BTD$_{11-12}$ values to the west of Bank's Island is largely associated with the presence of "liquid water" or "uncertain" phase clouds (see the Worldview classifications of Figure S1b).

3 Negative BTDs associated with liquid phase clouds in the inversion layer

130   The spectral properties of water clouds, for CODs that are typically >> than the weak DODs described above, will likely dominate the BTD$_{11-12}$ spectral signature of Asian dust or local dust that is not within the immediate range of its drainage basin source. We found numerous examples of the presence of low-level CM water-clouds characterized by strong COD and weakly to strongly negative BTD$_{11-12}$ values over the Beaufort Sea (illustrated by the COD >~ 5 and BTD$_{11-12}$>~ -1 °K May 29, 2005 case study of Figures S2 to S5). Given the arguments presented above on the general weakness of DODs and the likely absence

135   of any strong local dust source in the middle of the frozen Beaufort Sea, it is very unlikely that the massive region of negative BTD$_{11-12}$ values seen in cases such as that of Figure S3 could be attributed to the direct thermal influence of dust aerosols.

We found (over a 2011-2018 sampling period) persistent if irregular winter to spring (October to April) and summertime events of moderately negative MODIS BTD$_{11-12}$ values (-0.3 >~ BTD$_{11-12}$ >~ -0.8 °K) acquired near Barrow, where ground-based lidar and radar profiles indicated strong, super-unity CODs associated with physically thin, near-surface water clouds

140   (see the illustration and discussion of Figure S6 below). Such low-altitude mixed-phase (water mixed with ice) clouds have been reported in the literature: de Boers et al. (2009) and Shupe et al. (2015) provide lidar / radar supported illustrations of explicit mixed-phase events at Eureka and Barrow respectively[3]. The former paper reported a 4-year (2004-2007) frequency-of-occurrence (%) series (three-month-wide bins) of combined Barrow and Eureka results showing a general predominance of "SON" autumn bins (~ 10%) at <~ 1.5 km mean cloud-base-height[4] for single-layer, mixed-phase stratiform clouds. The latter

145   paper provided a 2-year Barrow climatology (which is more relevant to the Barrow-region focus of the analyses that follows) showing that the monthly occurrence (%) was highest in October (~ 40%) while being only moderate and of lower altitude from March (~ 10%) to ~ 25% in April and May (with a strong preponderance of sub-1-km liquid occurrence). Yi et al., 2019 reported comprehensive satellite-based (MODIS and CALIOP) water cloud ("Arctic fog"), March-to-October statistics for a large Arctic Ocean region roughly centered north of Barrow). Their water cloud limitation to fog (cloud base height = cloud

150   height – cloud thickness being < 1000 feet [300 meters]) was, however, rather restrictive with respect to the types of liquid cloud events that we investigate below (events requiring significant temperature slices of the Arctic inversion layer).

Nearly all our negative BTD$_{11-12}$ Barrow examples shared one feature that is rarely mentioned in typical BTD$_{11-12}$ literature; the ubiquitous and strong Arctic temperature-inversion up to altitudes ~ 1 km that occurs during the polar winter and summer (see Bradley et al., 1993 and Palo et al., 2017 for statistical summaries of the Arctic inversion layer). Inversion-layer cloud

---

[3] The reader will note that for the specific purposes of this paper we do not distinguish between liquid clouds and mixed phase clouds. Below we argue that the ice COD in mixed phase clouds is typically negligible compared to the liquid water COD

[4] With a plume thickness of <~ 600 m. These are the 3-year results for Eureka: the single Barrow year of 2004, with a SON occurrence of 26% was more coherent with the Shupe et al. results.

155 events are the most easily detectable instances of a fundamental principle; that a "warm-cloud" in the Arctic inversion layer (in an atmosphere clear of higher altitude clouds) transforms the more common negative-lapse-rate BTD_{11-12} signature from a generally positive to negative dependency with the degree of negativity being dependent (for a given surface emissivity, inversion-layer strength and water vapour load) on the COD and effective particle radius (Key, 2002; Liu et al., 2004).

We generated MODTRAN-simulated BTD_{11-12} vs BT_{11} graphics employing a variety of input parameters to encompass a wide

160 variety of COD and particle size conditions about the specific Figure S6, March 22, 2015 event at Barrow. The resulting BTD_{11-12} vs BT_{11} patterns are shown in Figure S8 while Table 1 presents a descriptive summary of both empirical and simulated patterns. The "convex downward" shape of a large-COD water cloud in an inversion layer will produce almost exclusively negative values that fundamentally depend on the COD = 0 and ∞ singularities on the BTD_{11-12} vs BT_{11} patterns of Figure S8b (while a high-altitude ice or liquid cloud will produce, as per Figure S8a, generally positive BTD_{11-12} values).

165

Table 1 - Empirical (E) & simulated (S) BT_{11-12} vs BT_{11} results for a variety of cloud or dust plumes embedded in positive temperature-lapse-rate (inversion layer) or negative lapse-rate regions. Blue, red and gold text refer respectively to water clouds, ice clouds and dust plumes.

Temperature lapse rate (dT/dz)	Emissivity Slope[1] ($d\varepsilon/d\lambda$)	BTD_{11-12} vs BT_{11} pattern	Cloud or dust plume & surface scenarios	Citations / comments
Negative	Negative	Convex upwards[1]	Low-altitude to mid-altitude water cloud	Baum et al. (2000) (**S**) [a], Key (2002) (**S**) [b]
Positive	Negative	Convex downwards[2]	Low-altitude (inversion layer) water clouds	This study [c] (**S & E**) Key (2002) [d] (**S**)
Negative	Negative	Convex upwards	High altitude ice clouds	This study (**S** [e] **& E**).
Positive	Negative	Convex downwards	Low-altitude (inversion layer) ice clouds	This study (**S** [f])
Negative	Positive [g]	Convex downwards	High altitude Asian dust plumes	Various (**S & E**) This study (**S**) [i]
Positive	Negative	Convex upwards	Low altitude (inversion layer) Asian dust plume parameters	This study (**S**)

[1] Otherwise known as concave downward. These curves generally (but not always) consist of positive BTD_{11-12} values
[2] Otherwise known as concave upward. These curves generally (but not always) consist of negative BTD_{11-12} values
[a] Surface to top-of-water-cloud temperature decrease of $\cong$ 297 to $\cong$ 284 °K (low altitude water cloud)
[b] Surface to top-of-water-cloud temperature decrease of 263.16 to 238.65 °K (mid altitude water cloud)
[c] Surface, top-of-inversion-layer-plume and top of high-altitude plume temperatures $\cong$ 256, 262 and 213 °K. See the captions of Figures S6 and S8 for details
[d] Surface to top-of-water-cloud temperature increase of 235.66 to 253.15 °K
[e] Same approximate values as footnote c. The high altitude ice-cloud literature is resplendent with convex-upward BTD_{11-12} vs BT_{11} examples (see, for example, Figure 3 of the tropical atmosphere simulation of Ackerman et al., 2010)
[f] Same approximate values as footnote c
[g] Han et al. (2012) point out that quartz is a major component of Asian dust. Quartz-dominated dust is generally characterized by positive $dk/d\lambda$ (resulting in positive $d\varepsilon/d\lambda$ according to our calculations)
[h] The dust parameterizations that we employed in our BTD_{11-12} vs BT_{11} simulations (see our dust refractive index survey in Appendix B) were sometimes referenced to results for African dust

[i] Many **S** & **E** examples in the literature of convex-upward BTD_{11-12} *vs* BT_{11} patterns (see, for e.g., Zhang et al., 2006). The generally negative nature of those patterns are a well known high altitude signature of Asian dust plumes.

Table glossary
E – empirical results, **S** – simulated results
ε – emissivity spectrum of a surface composed of water, ice or dust soil
$dk/d\lambda$ & $d\varepsilon/d\lambda$ – 11 to 12 μm spectral slope of respectively, the complex part of the refractive index & emissivity

Figure 1a shows a radar profile for the specific inversion-layer (Figure S8) Barrow illustration of the March 22, 2015 event (with Figure 1b providing a zoom of the radar profile in the inversion layer between ~ 0 and 2 km). Figure 1c shows both the MODIS-measured moderate-amplitude BTD_{11-12} values and the MODTRAN-simulated values (details in the figure caption). This demonstrates explicitly how (i) a warm liquid-water, inversion layer plume (whose lower and upper boundaries are explicitly shown in Figure S6 and Figure 1b) produces systematically varying BTD_{11-12} values that oscillate from negative to positive as driven by the negative BTD_{11-12} predominance of the inversion layer plume and positive BTD_{11-12} predominance of a cold (negative or normal lapse rate) ice-cloud around 6-km-altitude and (ii) that MODTRAN radiative transfer simulations were largely successful in capturing the BTD_{11-12} oscillations.
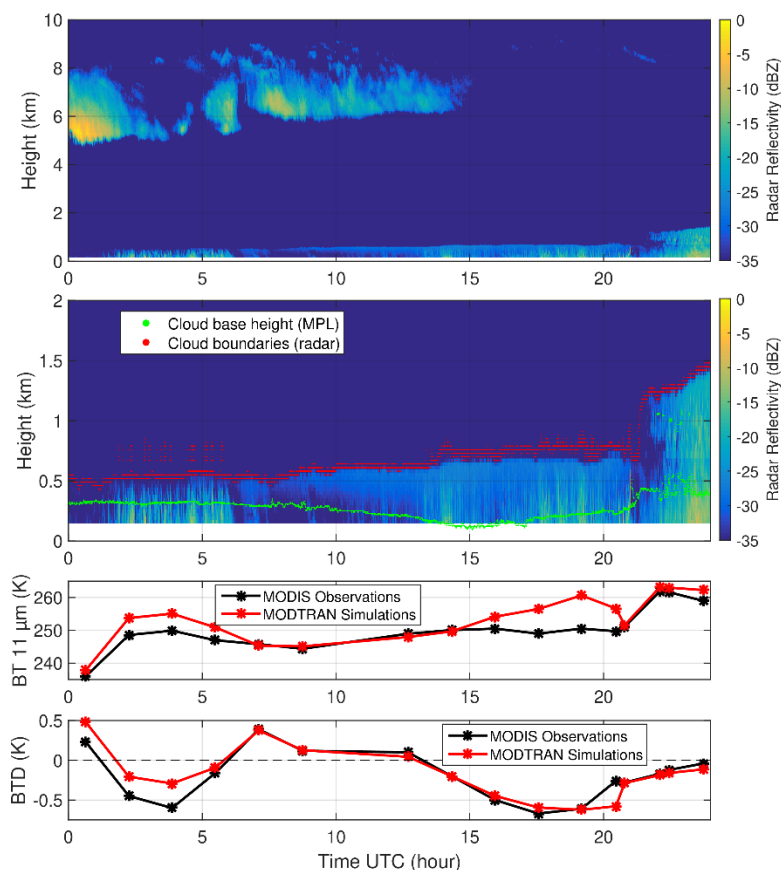
Figure 1 – Radar backscatter coefficient profiles acquired at the ARM Barrow site on Mar. 22, 2015 from (a) 0 to 10 km altitude (b) a zoom of (a) from 0 to 2 km altitude. The dynamical details of this event, including the juxtaposition of what we inferred to be a water-dominated, mixed-phase, inversion-layer plume (as measured by the combination of radar backscatter profile and NSHSRL backscatter and depolarization profiles) are given in the caption of Figure S6. Figure (c) shows both the MODIS-measured BTD_{11-12} values (for the pixel nearest to the Barrow site) and the MODTRAN-simulated values employing representative input parameters during that day (see the captions of Figure S6 and S7 for further details).

Specific details on the vertical extent of the mixed phase backscatter coefficient profile, their respective COD contributions and their relationship to the temperature (inversion layer) profile provided by the Barrow radiosonde profiles are presented in the discussion of Figure S6. In those details, we argue that the radar profiles provide key information about the upper boundary of the water / mixed phase plume (beyond the upper bound defined by the extinction limit of the lidar) and its attendant extension to altitudes where there was actually a strong temperature inversion.

The same (Table 1) inversion layer BTD_{11-12} convexity reversal should apply to warm, low-level ice-clouds in an Arctic inversion layer: however as shown in Figure S8b, the amplitude of the convex downward pattern can be insufficient to move the pattern into the negative BTD_{11-12} range. In any case, we did not, in our survey of significantly negative, near-Barrow BTD_{11-12} (MODIS) values, find any obvious lidar / radar retrievals dominated by synchronous, low-level, optically-thick ice-clouds in the inversion layer. This is not unexpected since the CODs of near-surface ice clouds are substantially smaller than those of water clouds (see Shonk et al., 2019 for a general statement and specific examples in the Dec. 29, 2006 Eureka case study of de Boer et al., 2009 as well as Sections 3d vs 4c of Zuidema et al., 2005 for a May 1 – 18, 1998 case study at a floating ice camp ~ 600 km northwest of Barrow). Morrison et al. (2012) also point out the dominance of water CODs over ice CODs across a 5 day (May 11 – 15, 2011) Eureka event and underscore the persistence of Arctic mixed-phase clouds in general. This dominance of water COD over ice COD was also found in our Figure 1 case study (see the caption of Figure S6 for details).

We would note that a convex-down to convex-up pattern reversal would occur for warm dust clouds located in an Arctic inversion layer: the generally negative contours for cold dust clouds would be transformed to positive contours (see Figure S8d) that would actually confound the classic negative BTD_{11-12} signature of cold, high-altitude dust clouds (see for example, Figures 3 (MODIS BTD_{11-12}) and Figure 4 (simulations) of Zhang et al., 2006). Support for this affirmation comes indirectly from Ranjbar et al. (2021): the lapse rate in the Lake Hazen case was, in all likelihood, a "classical" (inversion-free) rate of decreasing temperature with increasing altitude. This results in the negative BTD_{11-12} plume values reported in that paper (the defining BTD_{11-12} vs BTD_{11} pattern is more in the nature of the convex-down shapes of Figure S8c).

The overarching message of this section is that negative BTD_{11-12} values in the Arctic are not a unique signature of the pervasiveness of dust across the Arctic. The BTD_{11-12} signature of airborne dust in the inversion layer would generally be too weak to detect and of the wrong sign with respect to the classical negative signature of desert dust plumes in a normal lapse rate environment. DODs in the Arctic are generally too small to induce significant BTD_{11-12} amplitudes. The BTD_{11-12} signature of deposited dust can be significantly negative but, as suggested by our case study on snow deposition of local dust (see the following section), tend to be spatially limited to dust dominated regions of the drainage basin source.

4 RS detectability of dust impacts

An affirmation of the general marginality of airborne-dust RS detectability in the Arctic is not to say that the impacts of Asian or local dust are necessarily marginal in terms of satellite-based RS. The cumulative deposition of local dust associated with weak DODs can (as also noted by VCT) be substantial over seasonal or longer time scales with significant changes in surface reflectance (and attendant impacts on early snow melt coupled with a feedback effect of even greater reflectance changes). Ranjbar et al. (2021) showed a true-color May 18, 2019 reflectance image of northern Ellesmere Island with significant browning of the generally white ice/snow surface near known drainage basins (including Lake Hazen and the Fosheim Penninsula region of Eureka). Figure S9 shows, what we argue, are examples of dust deposition on snow or ice in the neighbourhood of drainage basins whose flow dynamics have induced local dust plumes. This illustrates how the accumulation of local dust deposition by dust plumes produces, (i) true-color images of significantly modified snow reflectance in the visible spectral region (<~ 60% average reflectance change; c.f. the "Dusty Snow" reflectance changes in the Figure 1a spectra of Painter et al., 2007) but only (ii) weakly positive BTD_{11-12} dust-deposition signatures near their drainage basin sources (while also showing that significantly negative BTD_{11-12} signatures do occur in what are likely the very localized pure dust regions of the drainage basins). This, as indicated in the legend of Figure S9, is likely a BTD_{11-12} difference that can be ascribed to a pure dust-surface emissivity difference between bands 11 and 12. These illustrations strongly suggest that, significantly negative signatures of dust on snow or ice are likely to be extremely limited in their spatial extent.

The reflectance effects associated with the deposition of Asian dust on snow are less evident. Asian dust deposition was detected by ground teams at higher altitudes (where sources of local dust would be unlikely) in the Mount Logan (Yukon) region of the St. Elias range during the strong April 2001 Asian dust event (Zdanowicz et al., 2006). The authors suggested that up to 45% of the airborne dust mass abundance was deposited in the snow (over a 9 day period) and that the mechanism for deposition was scavenging by snow flakes. MODIS corrected-true-color reflectance images show no obvious impact: this effort to determine an impact is not helped by these agents of deposition arguably confounding / camouflaging the darkening impact of dust. Zhao et al. (2022) employed a variety of ground- and satellite-based, passive and active RS data as well as surface nephelometer measurements of CM scattering coefficient to investigate the albedo (spectrally integrated reflectance) impact of dust deposition on snow during March 14, 2013 and April 20, 2015 Asian dust events over Alert (Nunavut) and Barrow, Alaska respectively[5]. The CM scattering coefficients coupled with estimates of the dust plume (mid-tropospheric) altitude over each site suggested direct deposition links between the dust plumes and the surface dust (they did not attempt to elaborate on any explanation of the deposition dynamics). A radiative transfer model was then employed by the authors to argue that daily dust deposition events could reduce snow surface (panchromatic) albedo by as much as 2.3% at Barrow and 1.9% at Alert. These albedo reductions would be quite substantial if dust depositions (in relatively unperturbed snow conditions) were allowed to accumulate over, for example the 9-day period of the April 2001 event. However, the simulations

---

[5] those two intensive-analysis days were supplemented by neighbouring days for which CM nephelometer measurements suggested the dust-event extended beyond those two core days.

of Groot Zwaaftink et al. (2016) on the substantially greater contribution of local Arctic dust (versus Asian or African dust) to dust deposition suggests that the mid-latitude (Asian and African) dust would, in general, play a secondary reflectance perturbation role compared to local dust.

245 A second substantial impact of Arctic dust particles is associated with their role as INP (ice nucleation particles) and their indirect effect on cloud dynamics. The core message of Kawai et al. (2023) was not a statement about the weak optical influence of local Arctic dust, but rather a simulation-based affirmation that local dust was the dominant INP source in the lower Arctic troposphere during summer and fall (much more dominant than Asian dust in general). A similar statement concerning the

250 dominance of local dust over Asian dust as INPs was made by Xi et al. (2022) based on INP (droplet freezing) measurements made near the source of local dust plumes at the sub-Arctic Lhù'ààn Mân' (Kluane Lake) site in the Canadian Yukon territory. Barr et al. (2023) reported on the greater INP activity of local dust (from glacial drainage basins on the southern Alaskan coast) relative to Arctic dust from low-latitude sources. Tobo et al. (2019) described the important role of local dust as an INP source in the Svalbard region and noted that the high ice nucleating ability of the local dust was likely governed by the presence of

255 organic matter. Shi et al. (2022) analyzed the radiative forcing impacts of local Arctic dust (what they called "HLD" for high-latitude dust as an acronym for Arctic dust whose source is in the Arctic). Their simulations (roughly supported by INP comparisons with measured INPs carried out at 9 stations) show, for example, that HLD INPs likely instigated a maximum depletion in the liquid water path (LWP) of mixed phase clouds in the fall season over the Canadian Arctic Archipelago (and lesser but still significant LWP changes during the summer and winter seasons). Those LWP depletions (~ 8 g-m^{-2}) amount to

260 water COD reductions of <~ 1.5 (at any wavelength for which the Mie extinction efficiency (Q) is ~ the optically large-particle asymptotic value of ~ 2). Such COD changes (along with their associated extinction coefficient profile change) would be readily detected using standard passive & active, satellite-based sensors (from the visible to the thermal IR).

5 Conclusions

We presented a variety of examples showing how direct RS-based estimates of CM Arctic dust were oftentimes excessively

265 large due to a failure in separating out the contribution of CM clouds (or cloud-like optical contributions). A particular emphasis was placed on a paper by Vincent (2018) who reported an optically strong airborne dust presence in the western Canadian Arctic that was ascribed to dust of Asian origin or dust from local sources. While we do not dispute the presence of both Asian and local dust in the Arctic, the direct RS detectability of airborne dust (attributed to satellite-measured values of significantly negative BTD$_{11-12}$ values) was likely misrepresented. While it is difficult to account for all examples of strongly

270 negative BTD$_{11-12}$, it is very unlikely that airborne dust plays a major RS role in any case other than plumes of strong DOD (> ~ 0.5). One, much more likely contributor would be water plumes (or, more generally stated, water dominated, mixed phase clouds) in the Arctic inversion layer.

The RS detectability of the impact of Arctic dust and notably Arctic dust from local drainage basin sources can, however, be of significance. Sustained dust deposition can substantially decrease the (visible to shortwave IR) snow and ice reflectance and

275 the attendant signal measured by satellite sensors (while significantly negative BTD_{11-12} values represent an extremely limited area according to our event level case studies). The reportedly stronger INP (Ice Nucleating Particle) role of local Arctic dust can, for example, induce significant changes in the properties of low-level mixed phase clouds (optical depth changes <~ unity) that can be readily detected by active and passive RS instruments. It is clearly critical that the distinction between the RS detectability of Arctic dust versus the RS detectability of the impacts of Arctic dust be understood if we are to properly account

280 for and model the radiative forcing impacts of dust in this climate sensitive region.

6 Appendices

Appendix A – Intensive optical parameters associated with local dust and Asian dust

A.1 DOD mass efficiency from local dust simulations of Kawai et al. (2023)

If V is the columnar, particle-volume abundance ρ is the dust particle density and A is the particle-number abundance then the

285 particle-mass abundance (A_m) in the case of the local dust simulations of Kawai et al. (2023) (KA) (or any unimodal particle-volume or particle-mass distribution) is given by;

$$A_m = \rho V \cong \rho \frac{4}{3} \pi r_{eff}^3 A \qquad (A1a)$$

$$A \cong \frac{A_m}{\rho \frac{4}{3} \pi r_{eff}^3} \cong \frac{A_m}{m} \qquad (A1b)$$

where the concept of intensive parameters averaged over a unimodal particle size distribution is discussed, for example, in

290 O'Neill et al. (2005). If the dust extinction cross section is σ and Q is the dust extinction efficiency, then the dust optical depth (DOD) is;

$$\tau \cong \sigma A \cong \sigma \frac{A_m}{\rho \frac{4}{3} \pi r_{eff}^3} = Q \pi r_{eff}^2 \frac{A_m}{\rho \frac{4}{3} \pi r_{eff}^3} = \frac{Q A_m}{\frac{4}{3} \rho r_{eff}} \qquad (A2)$$

Employing the mean r_{eff} of 2.7 µm from the Kok (2011) (Kok) distributions (see Appendices A.3 and A.4) yields $x_{eff} = 2 \pi r_{eff} / \lambda = 33$ for $\lambda = 0.5$ µm. Q is ~ 2.3 for values of x_{eff} ~ 10 (Hinds, 1999)[6] and refractive indices representative of

295 dust[7]. Employing the MITR[8] density of 2.6 g-cm^{-3} → 2.6 × 10^3 mg / (10^{-2} m)^3 → 2.6 × 10^9 mg/m^3 yields;

$$\tau \sim \frac{2.3 A_m}{\frac{4}{3} (2.6 \times 10^9) \text{ mg/m}^3 \times (2.65 \times 10^{-6}) \text{ m}} \sim 0.250 \times 10^{-3} \text{ (mg/m}^2)^{-1} A_m \qquad (A3)$$

One can define a "DOD mass efficiency" × 10^4 (DOD per unit columnar mass abundance) as;

$$DOD_m \times 10^4 = \frac{\tau}{A_m} \sim 2.5 \text{ (mg/m}^2)^{-1} \qquad (A4)$$

---

[6] Figure 16.2: note that Hinds' diameter-based size parameter $(\alpha) = 2 \times$ our radius-based size parameter of x

[7] 1.53 – 0.0078i for the MITR ("Mineral transported") class of dust (the "opdat" directory of the OPAC package). Hess et al.'s MITR density transforms as 2.6 g/cm^3 = 2.6 × 10^3 mg/(10^{-2} m)^3 = 2.6 × 10^9 mg/m^3

[8] Optical and µphysical parameters are listed in Table 1c of Hess et al. (1998).

A.2 Simulated DODs extracted from KA's DOD_m value

A_m is $\cong$ a maximum of $10^{(1+2/3)} = 46.4$ mg/m^2 at the beginning of the red bar in KA's Figure 1(a) color legend. This yields a maximum τ (DOD) value of $\sim 2.5 \times 10^{-4}$ (mg/m^2)$^{-1}$ $\times$ 46.4 mg/m^2 = 0.012. A more spatially explicit comparison between KA's annual-means and AeF's climatology are the numbers in Table A1 below. AeF's monthly-binned CM AOD geometric averages would include local dust, springtime Asian dust and open-water sea-salt.

Table A1 – Local dust AODs (yearly averages) derived from the mass abundances of KA's Figure 1

Site	Lat., Long.	$DOD_m \times 10^4$ [(mg/m^2)$^{-1}$]	A_m [mg/m^2]	Computed DOD (τ)
Resolute Bay	75°N, 95°W	2.5	14.68	0.0037
Eureka	80°N, 86°W	2.5	0.32	0.000079
Thule	77°N, 69°W	2.5	3.16	0.00079
Hornsund	77°N, 16°E	2.5	6.81	0.0017

A.3 Effective radius relationships for spherical particles

The effective radius for spherical particles is defined by Hansen & Travis (1974) (HT) as:

$$r_{eff} = \frac{\int r^3 \frac{dn}{d \ln r} d \ln r}{\int r^2 \frac{dn}{d \ln r} d \ln r} = \frac{\int (D/2)^3 \frac{dn}{d \ln D} d \ln D}{\int (D/2)^2 \frac{dn}{d \ln D} d \ln D} = \frac{1}{2} \frac{\int D^3 \frac{dn}{d \ln D} d \ln D}{\int D^2 \frac{dn}{d \ln D} d \ln D} = \frac{1}{2} D_{eff} \qquad (A5)$$

where the very last relation amounts to a definition of D_{eff}. Equation (A5) can then be recast in terms of total particle-surface and particle-volume concentration:

$$D_{eff} = \frac{\frac{2^3}{\frac{4}{3}\pi} \int \frac{4}{3}\pi \left(\frac{D}{2}\right)^3 \frac{dn}{d \ln D} d \ln D}{\frac{2^2}{\pi} \int \pi \left(\frac{D}{2}\right)^2 \frac{dn}{d \ln D} d \ln D} = \frac{3}{2} \frac{\int \frac{dv}{d \ln D} d \ln D}{\int \frac{ds}{d \ln D} d \ln D} = \frac{3}{2} \frac{v}{s} \qquad (A6a)$$

From equation (A5) the effective diameter can be recast as:

$$D_{eff} = \frac{3}{2} \frac{\int \frac{4}{3}\left(\frac{D}{2}\right) \frac{ds}{d \ln D} d \ln D}{\int \frac{ds}{d \ln D} d \ln D} = \frac{\int D \frac{ds}{d \ln D} d \ln D}{\int \frac{ds}{d \ln D} d \ln D} = \frac{\int D \frac{ds}{d \ln D} d \ln D}{\int \frac{ds}{d \ln D} d \ln D} = \langle D \rangle_{\omega = ds/d \ln D} \qquad (A6b)$$

the weighted mean of D where the weight $\omega = ds/d \ln D$. Ginoux (2003) argues that the shape of dust particles are, in general, better represented by prolate ellipsoids (see the following section).

A.4 Computation of D_{eff}

Kawai et al. (2023) employed Kok's particle-volume distribution as the basis of their simulations (ultimately it was the starting point of their computations of seasonally averaged particle-mass columnar densities). Kok's particle-volume size distribution (his equation (6)) is related to his particle-number size distribution (his equation (5)) by $dV_d/dlnD_d = C_N/C_V D_d^3 dN_d/dlnD_d$. We can (dropping his "d" for dust subscript, using lower case letters for these point-volume parameters and $\tilde{n}$ and $\tilde{v}$ for for their "normalized" distributions) recast this as;

$$d\tilde{v}/dlnD = C_N/C_V \, [3/(4\pi) \, 2^3] \, [(4/3)\pi \, (D/2)^3] \, d\tilde{n}/dlnD$$
$$= (\, C_N/C_V \, 6/\pi) v_{sp}(D) \, d\tilde{n}/dlnD$$
$$= C_{Kok} v_{sp}(D) \, d\tilde{n}/dlnD \quad (A7)$$

325   where $v_{sp}(D) = (4/3)\pi \, (D/2)^3$ is the volume of a spherical particle of radius $D/2$ and $C_{Kok} = C_N/C_V \times 6/\pi$. However C_{Kok} ($= 0.144$ for Kok's C_N and C_V values of 0.9539 and 12.62 µm respectively) is not close to unity as would be expected for small dust particles. Equation (A7) is apparently the correct inter-distribution relationship between Kok's (Figure 6) "normalized" number and "normalized" volume size distributions (as verified by the fact that the black, solid-line, open-circle ($C_{Kok} v_{sp}(D) \, d\tilde{n}/dlnD$) curve is very close to Kok's gold, solid-line full-circle curve ($d\tilde{v}/dlnD$) in Supplementary material

330   ("Local_dust_PSDs.xlsx")).

However equation (A6a) applied to Kok's normalized distributions give unrealistic estimates of the effective radius (0.78 µm)[9]. Those normalized distributions were not defined and so we have to tentatively conclude that the normalization precluded the application of equation (A6a)[10]. Dust particles are not sufficiently large to have substantial non-sphericity effects and so one expects the departure of C_{Kok} from unity to be relatively small. Ginoux (2003) cited Okada et al. (2001) to indicate that

335   dust particles near their source (Chinese desert sites) displayed an ellipsoid aspect ratio (λ) of ~ 1.5 and that moderately higher values of 2 showed no significant departure from sphericity (their Figure 5, for example, shows that simulated particle volume distributions for λ = 2 were quite close to the spherical-particle AERONET inversions for 6 sites near or in the desert sources of dust). Accordingly we can, in general, treat dust particles as being approximately spherical ($d\tilde{v}/dlnD \sim v_{sp}(D) \, d\tilde{n}/dlnD$) and the light-grey broken-line open-circles in the Supplementary material ("Local_dust_PSDs.xlsx") represents the appropriate

340   distribution[11] for the employment of equation (A6a). This yields a D_{eff} value of 5.40 µm ($r_{eff} = 2.70$ µm).

A.5 KA-model underestimation of DOD (vs CALIOP DOD) is irrelevant to DOD_m estimation

Figure S4 of KA's supplementary material shows that their simulated 550 nm "annual-mean zonally averaged dust AOD" significantly underestimate the DOD relative to the CALIOP 532 nm DOD[12]. Table A2 shows the DODs (τ) computed from KA's Figure 1 at AeF's AERONET sites. The computations include a trial "correction" of the simulated DODs (DOD - ΔDOD)

---

[9] Versus, for example, a volume-weighted geometric mean diameter (VMD) of 6.51 µm (the AERONET-inversion type of calculation)

[10] Meaning, that Kok's normalized distributions were not equally proportional to their physical representations (the physical representations being symbolized by the hatless variables in Section A.3)

[11] Meaning that we treat the distributions as being spherical-particle distributions

[12] ΔDOD ~ - 0.005 at the 75°N lat. of Resolute Bay and ~ - 0.003 at the near 80°N lat. of Eureka, Thule and Hornsund: values were eyeballed from KA's Figure S4 ((-1) × [CALIOP curve – red KA simulation curve]). One cannot, of course exclude the opposing hypothesis that CALIOP DODs were overestimated.

to yield values that are ~ CALIOP DODs. This correction increases $DOD_m \times 10^4$ from 2.50 to ~ values computed for the April

2001 Asian dust event over Mount Logan (see Section A.6 for Mount Logan details)[13].

The problem with that computation is that the required increase in simulated DODs necessarily requires a proportional increase

in A_m if the change is assumed to be due to extensive-parameter differences (if the implied constancy of DOD_m in equation

(A4) is accepted as being largely true).

350

Table A2 – Computed DOD values (DOD (τ)) employing the nominal $\boldsymbol{DOD_m}$ value of equation (4) above and modified DOD values (DOD
- ΔDOD) computed by "correcting" the nominal DOD values to the CALIOP DOD values from KA's Figure S4.

Site	Lat., long.	$DOD_m \times 10^4$ [(mg/m^2)$^{-1}$]	Computed DOD (τ)	DOD - ΔDOD[a]	$DOD_m \times 10^4$ [(mg/m^2)$^{-1}$]
Resolute Bay	75°N, 95°W	2.50	0.0037	0.0087	5.91
Eureka	80°N, 86°W	2.50	0.000079	0.0031	97.0
Thule	77°N, 69°W	2.50	0.00079	0.0038	12.0
Hornsund	77°N, 16°E	2.50	0.0017	0.0047	6.91
[a] The simulations appear to underestimate the CALIOP "truth": their (ΔDOD) bias is accordingly negative.					

A.6 Comparison of DOD mass efficiencies (local dust vs Asian dust)

The daily averaged value of the NAAPS DOD over Mount Logan during the Asian dust event on the single day of April 14,

355 2001 is 0.19[14] (see the NAAPS results of Table A3 below). The corresponding (very approximate) "daily dust column loading"

from "Figure 11 of Gong et al. (2003) is[15] ~ $100 \times 2^{\pm 1}$ mg m^{-2}. This yields a an Asian dust DOD mass efficiency $\times 10^4$ (DOD_m

$\times 10^4$) = $19 \times 2^{\pm 1}$ (mg m^{-2})$^{-1}$. The local $DOD_m \times 10^4$ value of 2.50 (mg/m^2)$^{-1}$ from above is significantly less than this value:

the difference is due to a combination of the greater Mie kernel[16] of the approximately 1.3 µm radius Asian dust (AeF) vs the

2.7 µm radius assumed for local dust[17] and the smaller columnar mass of Asian dust in the denominator of the DOD_m

360 expression of equation (A4).

Table A3 – Visually determined April, 11 to 19, 2001 NAAPS DODs[18] at Mount Logan, YK (60° 34' N, 140° 24' W). The DOD values are
the midpoints of the NAAPS color-scale bins. If there is no NAAPS DOD (no NAAPS dust at the position of Mount Logan) then the bin is
assigned a value of 0.0 (0.15 if the edge of the 0.15-valued dust plume cannot be visually separated from the position of Mount Logan). If

---

[13] This "corrections" of the simulations appeared to be necessary because no matter how much the Mount Logan results were
tweaked as a function of their inherent display errors, no acceptable agreement with the low DOD_m values of the uncorrected
KA simulations could be achieved.

[14] https://www.nrlmry.navy.mil/aerosol_temp/loop_html/aer_globaer_noramer_loop_2001041818.html

[15] This was the most precise that could be achieved with a figure that is difficult to see (the other 3 cross-haired days yield
very uncertain values of daily dust column loading)

[16] See Figure 1 of O'Neill et al. (2023) for a definition and graphical interpretation of the Mie kernel

[17] <D$_{eff}$>/2 from the value given above in Section A.4

[18] https://www.nrlmry.navy.mil/aerosol-
bin/aerosol/display_directory_all_t.cgi?DIR=/web/aerosol/public_html/globaer/ops_01/noramer/200104&TYPE=

365 the position of Mount Logan is, in any way, blocked by the presence of a simulated NAAPS dust plume, then Mount Logan is assigned the DOD value of that plume. The arithmetic average of all the DOD values below is <DOD> = 0.13

ddhh (UT)	DOD$_{bin center}$	ddhh (UT)	DOD$_{bin center}$	ddhh (UT)	DOD$_{bin center}$
1100	0.0	1400	0.0	1700	0.15
1106	0.0	1406	0.15	1706	0.15
1112	0.0	1412	0.3	1712	0.15
1118	0.0	1418	0.3	1718	0.15
1200	0.0	1500	0.3	1800	0.15
1206	0.15	1506	0.3	1806	0.15
1212	0.15	1512	0.3	1812	0.0
1218	0.15	1518	0.3	1818	0.0
1300	0.15	1600	0.15	1900	0.15
1306	0.0	1606	0.15	1906	0.15
1312	0.15	1612	0.15	1912	0.0
1318	0.15	1618	0.15	1918	0.0

Appendix B – Optical constants

B.1 Survey of dust refractive indices (11 and 12 µm)

This survey was carried to support the refractive index decisions employed in the generation of Figure 1 of the main text and

370 Figure S8 of the Supplementary material ("Supp_figures.pptx"). Table B1 is a concise summary of the survey results.

Table B1: Survey of published dust / sand refractive indices (n-ik) and complementary data at 11 and 12 µm

Source	Users	n (11 µm)[c]	n (12 µm)[c]	k (11 µm)[c]	k (12 µm)[c]	Comment
Koepke et al. (1997)[a] [19]	Li et al., (2018)	1.829	1.774	0.209	0.428	*"Substance": "Sand"* *"Type": "Quartz and clay"*
Rothman et al. (2009)		1.6[d]	2.0[d]	0.02[d]	0.1[d]	"HITRAN Quartz"[b] Rothman citation is from Han et al. (2012)
Sadrian et al. (2023)		1.595	1.510	0.085	0.005	Taklimakan, China (sample S1014 for e.g.) Carbonate absorption was identified in S1014
Volz (1972)[20]	Table 3 of Zhang et al. (2006)[e]	1.618	1.548	0.105	0.095	*"Substance": "Dust"* *"Sample": "Rainout dust"* No comment about the composition of the dust
Volz (1973)[21]	Gu et al. (2003)	1.825	1.778	0.302	0.181	*"Substance": "Sand"* *"Type": "Saharan sand", "Sample": "Barbados"* From Volz (1973): "clay, illite, and kaolinite along with traces of quartz"

[19] https://eodg.atm.ox.ac.uk/ARIA/data?Sand_and_Dust/Sand/Quartz_and_clay_(Koepke_et_al._1997)/sand_koepke_1997.ri
[20] https://eodg.atm.ox.ac.uk/ARIA/data?Sand_and_Dust/Dust/Rainout_dust_(Volz_1972)/dust_volz_1972.ri
[21] https://eodg.atm.ox.ac.uk/ARIA/data?Sand_and_Dust/Sand/Saharan_sand/Barbados_(Volz_1973)/sand_volz_1973.ri

Wald et al. (1998)				no k data but $\varepsilon = 0.82$	no k data but $\varepsilon = 0.90$	Case of "pure quartz". Smaller particles (0 - 70 µm diameter[f]) show a significantly greater positive $d\varepsilon/d\lambda$ (emissivity (ε)[g] slope from 11 to 12 µm)

[a] the Koepke & Volz links: EODG (Earth Obs. Data Group), Aerosol Refractive Index Archive (consulted Oct. 4, 2023).The italicized text are the labels from that site. These numbers are very close to the OPAC numbers (see section "Row removed from Table B1" below)
[b] "HITRAN is also tested because quartz is one of the major components of Asian dust [Jeong, 2008]" (Han et al., 2012). This quote is a statement about the % weight of components in bulk samples of Asian dust (see Jeong, 2008).
[c] Precisely 11.03 and 12.02 µm respectively for all table entries except the OPAC and HITRAN values.
[d] These are coarse visual estimates from Figure 2 of Han et al. (2012).
[e] The n and k values of their Table 3 "Dust-like" component are those of Volz (1972) and not, as claimed, Koepke et al. (1997). Their reference to Gu et al. (2003) as a data source is more directly a reference to Volz et al. (1973)
[f] The authors state (in the discussion of their Figure 1 ε spectra) that: "Because the samples were made by grinding, the 0-75 µm sample is numerically dominated by < 5 µm diameter particles"
[g] and thus, perhaps, a greater absorption coefficient and thus k slope.

7 Author contribution

Norm T. O'Neill: Writing – original draft preparation – review & editing, Conceptualization, Methodology, Investigation, Formal analysis, Visualization, Validation, Project administration, Data curation, Funding acquisition, Resources. **Keyvan Ranjbar:** Writing – review & editing, Conceptualization, Investigation, Software, Formal analysis, Visualization, Validation. **Liviu Ivănescu:** Writing – review & editing, Conceptualization, Investigation, Software, Formal analysis, Visualization, Validation. **Yann Blanchard:** Writing – review & editing, Conceptualization, Investigation, Software, Formal analysis, Visualization, Validation. **Seyed Ali Sayedain:** Writing – review & editing, Conceptualization, Validation. **Yasmin AboEl-Fetouh:** Writing – review & editing, Conceptualization.

8 Competing interests

The authors declare that they have no conflict of interest.

9 Acknowledgements

This work was supported by CANDAC (the Canadian Network for the Detection of Atmospheric Change) via the Canadian NSERC (National Sciences and Engineering Research Council) CREATE Training Program in Arctic Atmospheric Science, as well as by grant 21SUASACOA from the ESS-DA program of the Canadian Space Agency (CSA). Financial support was also provided by O'Neill's NSERC Discovery Grant. With respect to the Barrow (Utqiagvik) North Slope Alaska (NSA) analysis: data were obtained from the Atmospheric Radiation Measurement (ARM) user facility, a U.S. Department of Energy (DOE) office of science user facility managed by the Biological and Environment Research program. Valuable in-kind support was provided respectively by the AEROCAN network of Environment and Climate Change Canada (ECCC) and the NASA

AERONET network. We also acknowledge the efforts of Antonis Gkikas of the National Observatory of Athens (NOA) Institute for Astronomy, Astrophysics, Space Applications and Remote Sensing (IAASARS) in providing detailed MIDAS DOD retrievals and uncertainties over the Arctic.

10 Acronym and symbol glossary

AERONET	World-wide NASA network of combined sunphotometer / sky-scanning radiometers manufactured by CIMEL Éléctronique. See AERONET website[22] for documentation and data downloads
AHSRL	Arctic High Spectral Resolution Lidar
AOD	The community uses "AOD" to represent anything from nominal aerosol optical depth which hasn't been cloud-screened to the conceptual (theoretical) interpretation of aerosol optical depth. In this paper we use it in the latter sense and apply adjectives as required.
Aqua	Aqua passes south to north over the equator in the afternoon (originally known as EOS PM-1)
ARM	Atmospheric Radiation Measurements
β	Backscatter cross section (m^{-1} sr^{-1})
BT, BTD	Brightness Temperature, Brightness Temperature Difference
CM	Coarse mode (generally super-micron)
COD	Cloud Optical Depth
DOD	Dust Optical Depth
FM	Fine mode (generally sub-micron)
HLD	High Latitude Dust
HYSPLIT	HYbrid Single-Particle Lagrangian Integrated Trajectory
INP	Ice Nucleation Particle
KAZRGE	Ka ARM Zenith Radar (KAZR)[23] GEneral mode. Zenith pointing Doppler radar operating at 35 GHz (8.6 mm)
LWP	Liquid Water Path
MISR	Multi-angle Imaging SpectroRadiometer
MODIS	Moderate Resolution Imaging Spectroradiometer
NSHSRL	North Slope High Spectral Resolution Lidar

---

[22] https://aeronet.gsfc.nasa.gov/
[23] https://adc.arm.gov//metadata/html/nsakazrgeC1.b1.html

| Terra | Terra passes from north to south across the equator in the morning |
| TIR | Thermal InfraRed |

References

AboEl-Fetouh, Y., O'Neill, N. T., Ranjbar, K., Hesaraki, S., Abboud, I., & Sobolewski, P. S.: Climatological-Scale Analysis of Intensive and Semi-intensive Aerosol Parameters Derived From AERONET Retrievals Over the Arctic. *Journal of Geophysical Research: Atmospheres*, *125*(10). https://doi.org/10.1029/2019jd031569, 2020.

Barr, S. L., Wyld, B., McQuaid, J. B., Neely, R. R., & Murray, B. J.: Southern Alaska as a source of atmospheric mineral dust and ice-nucleating particles. *Science Advances*, *9*(33), 1–12. https://doi.org/10.1126/sciadv.adg3708, 2023.

Bowen, M., & Vincent, R. F.: An assessment of the spatial extent of polar dust using satellite thermal data. *Scientific Reports*, *11*(1), 1–9. https://doi.org/10.1038/s41598-020-79825-7, 2021.

Bradley, R. S., Keimig, F. T., & Diaz, H. F.: Recent changes in the North American Arctic boundary layer in winter. *Journal of Geophysical Research*, *98*(D5), 8851–8858. https://doi.org/10.1029/93JD00311, 1993.

de Boer, G., Eloranta, E. W., & Shupe, M. D.: Arctic mixed-phase stratiform cloud properties from multiple years of surface-based measurements at two high-latitude locations. *Journal of the Atmospheric Sciences*, *66*(9), 2874–2887. https://doi.org/10.1175/2009JAS3029.1, 2009.

Eck, T. F., Holben, B. N., Reid, J. S., Sinyuk, A., Hyer, E. J., O'Neill, N. T., Shaw, G. E., Vande Castle, J. R., Chapin, F. S., Dubovik, O., Smirnov, A., Vermote, E., Schafer, J. S., Giles, D., Slutsker, I., Sorokine, M., & Newcomb, W. W.: Optical properties of boreal region biomass burning aerosols in central Alaska and seasonal variation of aerosol optical depth at an Arctic coastal site. *Journal of Geophysical Research Atmospheres*, *114*(11), 1–14. https://doi.org/10.1029/2008JD010870, 2009.

Ginoux, P.: Effects of nonsphericity on mineral dust modeling. *Journal of Geophysical Research: Atmospheres*, *108*(2). https://doi.org/10.1029/2002jd002516, 2003.

Gkikas, A., Proestakis, E., Amiridis, V., Kazadzis, S., Di Tomaso, E., Tsekeri, A., Marinou, E., Hatzianastassiou, N., & Pérez Garciá-Pando, C.: ModIs Dust AeroSol (MIDAS): A global fine-resolution dust optical depth data set. *Atmospheric Measurement Techniques*, *14*(1), 309–334. https://doi.org/10.5194/amt-14-309-2021, 2021.

Gong, S. L., Zhang, X. Y., Zhao, T. L., McKendry, I. G., Jaffe, D. A., & Lu, N. M.: Characterization of soil dust aerosol in China and its transport and distribution during 2001 ACE-Asia: 2. Model simulation and validation. *Journal of Geophysical Research: Atmospheres*, *108*(9), 1–19. https://doi.org/10.1029/2002jd002633, 2003.

Groot Zwaaftink, C. D., Grythe, H., Skov, H., & Stohl, A.: Substantial contribution of northern high-latitude sources to mineral dust in the Arctic. *Journal of Geophysical Research*, *121*(22), 13,678-13,697. https://doi.org/10.1002/2016JD025482, 2016.

Gu, Y., Rose, W. I., & Bluth, G. J. S.: Retrieval of mass and sizes of particles in sandstorms using two MODIS IR bands: A case study of April 7, 2001 sandstorm in China. *Geophysical Research Letters*, *30*(15), 1998–2001. https://doi.org/10.1029/2003GL017405, 2003.

Han, H. J., Sohn, B. J., Huang, H. L., Weisz, E., Saunders, R., & Takamura, T.: An improved radiance simulation for hyperspectral infrared remote sensing of Asian dust. *Journal of Geophysical Research Atmospheres*, *117*(9), 1–10. https://doi.org/10.1029/2012JD017466, 2012.

Hansen, J.E., Travis, L.D.: Light scattering in planetary atmospheres, *Space Sci Rev* **16**, 527–610, https://doi.org/10.1007/BF00168069, 1974.

Hess, M., Koepke, P., & Schult, I.: Optical Properties of Aerosols and Clouds: The Software Package OPAC. *Bulletin of the American Meteorological Society*, *79*(5), 831–844. https://doi.org/10.1175/1520-0477(1998)079<0831:OPOAAC>2.0.CO;2, 1998.

Hildner, R. D.: Understanding Aerosol-Cloud Interactions in Ice Saturated Environments using AHSRL, CALIOP and Trajectory Cluster Analysis, 2nd Symposium on Aerosol-Cloud-Climate Interactions, Jan 20, 2010.

Hinds, W. C.: *Aerosol technology : properties, behavior, and measurement of airborne particles*. John Wiley & Sons; 1999, 483 pp., 1999.

Hsu, N. C., Gautam, R., Sayer, A. M., Bettenhausen, C., Li, C., Jeong, M. J., Tsay, S. C., & Holben, B. N.: Global and regional trends of aerosol optical depth over land and ocean using SeaWiFS measurements from 1997 to 2010. *Atmospheric Chemistry and Physics*, *12*(17), 8037–8053. https://doi.org/10.5194/acp-12-8037-2012, 2012.

Jeong, G. Y.: Bulk and single-particle mineralogy of Asian dust and a comparison with its source soils, J. Geophys. Res., 113, D02208. https://doi.org/10.1029/2007JD008606, 2008.

Kawai, K., Matsui, H., & Tobo, Y.: Dominant Role of Arctic Dust With High Ice Nucleating Ability in the Arctic Lower Troposphere. *Geophysical Research Letters*, *50*(8), 1–10. https://doi.org/10.1029/2022GL102470, 2023.

Key, J.: The Cloud and Surface Parameter Retrieval (CASPR) System for Polar AVHRR: Users Guide. *Cooperative Institute for Meteorological Satellite Studies, University of Wisconsin*, *1225*, 33–69, 2002.

Koepke, P., Hess, M., Schult, I., Shettle, E.P.:Global Aerosol Data Set. Report No. 243, ISSN: 0937-1060. Max-Planck-Institut für Meteorologie, Hamburg, 1997.

Kok, J. F.: A scaling theory for the size distribution of emitted dust aerosols suggests climate models underestimate the size of the global dust cycle. *Proceedings of the National Academy of Sciences of the United States of America*, *108*(3), 1016–1021. https://doi.org/10.1073/pnas.1014798108, 2011.

Li, J., Wong, M. S., Wai, K. M., & Lee, K. H.: Characterization of Asian Dust Storms by MTSAT Satellite Retrievals. *5th International Workshop on Earth Observation and Remote Sensing Applications, EORSA 2018 - Proceedings*, 1–5. https://doi.org/10.1109/EORSA.2018.8598641, 2018.

Liu, Y., Key, J. R., Frey, R. A., Ackerman, S. A., & Menzel, W. P.: Nighttime polar cloud detection with MODIS. *Remote Sensing of Environment*, *92*(2), 181–194. https://doi.org/10.1016/j.rse.2004.06.004, 2004.

Meinander, O., Dagsson-Waldhauserova, P., Amosov, P., Aseyeva, E., Atkins, C., Baklanov, A., Baldo, C., Barr, S. L., Barzycka, B., Benning, L. G., Cvetkovic, B., Enchilik, P., Frolov, D., Gassó, S., Kandler, K., Kasimov, N., Kavan, J., King, J., Koroleva, T., Krupskaya, V., Kulmala, M., Kusiak, M., Lappalainen, H. K., Laska, M., Lasne, J., Lewandowski, M., Luks, B., McQuaid, J. B., Moroni, B., Murray, B., Möhler, O., Nawrot, A., Nickovic, S., O'Neill, N. T., Pejanovic, G., Popovicheva, O., Ranjbar, K., Romanias, M., Samonova, O., Sanchex-Marroquin, A., Schepanski, K., Semenkov, I., Sharapova, A., Shevnina, E., Shi, Z., Sofiev, M., Thevenet, F., Thorsteinsson, T., Timofeev, M., Silas Umo, N., Uppstu, A., Urupina, D., Varga, G., Werner, T., Arnalds, O., Vukovic Vimic, A.: Newly identified climatically and environmentally significant high-latitude dust sources. Atmospheric Chemistry and Physics, 22(17), 11889–11930, https://doi.org/10.5194/acp-22-11889-2022, 2022.

Morrison, H., De Boer, G., Feingold, G., Harrington, J., Shupe, M. D., & Sulia, K.: Resilience of persistent Arctic mixed-phase clouds. *Nature Geoscience*, *5*(1), 11–17. https://doi.org/10.1038/ngeo1332, 2012.

Okada, K., Heintzenberg, J., Kai, K., & Qin, Y.: Shape of atmospheric mineral particles collected in three Chinese arid-regions. *Geophysical Research Letters*, *28*(16), 3123–3126. https://doi.org/10.1029/2000GL012798, 2001.

O'Neill, N. T., Baibakov, K., Hesaraki, S., Ivanescu, L., Martin, R. V., Perro, C., Chaubey, J. P., Herber, A., & Duck, T. J.: Temporal and spectral cloud screening of polar winter aerosol optical depth (AOD): Impact of homogeneous and inhomogeneous clouds and crystal layers on climatological-scale AODs. *Atmospheric Chemistry and Physics*, *16*(19), 12753–12765. https://doi.org/10.5194/acp-16-12753-2016, 2016.

O'Neill, N. T., Ranjbar, K., Ivanescu, L., Eck, T. F., Reid, J. S., Giles, D. M., Pérez-Ramírez, D., & Chaubey, J. P.: Relationship between the sub-micron fraction (SMF) and fine-mode fraction (FMF) in the context of AERONET retrievals. *Atmospheric Measurement Techniques*, *16*(4), 1103–1120. https://doi.org/10.5194/amt-16-1103-2023, 2023.

O'Neill, N. T., Thulasiraman, S., Eck, T. F., & Reid, J. S.: Robust optical features of fine mode size distributions: Application to the Québec smoke event of 2002. *Journal of Geophysical Research: Atmospheres*, *110*(11), 1–16. https://doi.org/10.1029/2004JD005157, 2005.

Painter, T. H., Barrett, A. P., Landry, C. C., Neff, J. C., Cassidy, M. P., Lawrence, C. R., McBride, K. E., & Farmer, G. L.: Impact of disturbed desert soils on duration of mountain snow cover. *Geophysical Research Letters*, *34*(12), 1–6. https://doi.org/10.1029/2007GL030284, 2007.

Palo, T., Vihma, T., Jaagus, J., & Jakobson, E.: Observations of temperature inversions over central Arctic sea ice in summer. *Quarterly Journal of the Royal Meteorological Society*, *143*(708), 2741–2754. https://doi.org/10.1002/qj.3123, 2017.

Ranjbar, K., O'Neill, N. T., & Aboel-Fetouh, Y.: Comment on "Short-cut transport path for Asian dust directly to the Arctic: A case Study" by Huang et al. (2015) in Environ. Res. Lett. *Atmospheric Chemistry and Physics*, *22*(3), 1757–1760. https://doi.org/10.5194/acp-22-1757-2022, 2022.

Ranjbar, K., O'Neill, N. T., Ivanescu, L., King, J., & Hayes, P. L.: Remote sensing of a high-Arctic, local dust event over Lake Hazen (Ellesmere Island, Nunavut, Canada). *Atmospheric Environment*, *246*, 118102. https://doi.org/10.1016/j.atmosenv.2020.118102, 2021.

Rothman, L. S., Gordon, I. E., Barbe, A., Benner, D. C., Bernath, P. F., Birk, M., Boudon, V., Brown, L. R., Campargue, A., Champion, J. P., Chance, K., Coudert, L. H., Dana, V., Devi, V. M., Fally, S., Flaud, J. M., Gamache, R. R., Goldman, A., Jacquemart, D., … Vander Auwera, J.: The HITRAN 2008 molecular spectroscopic database. *Journal of Quantitative*

495   *Spectroscopy and Radiative Transfer*, *110*(9–10), 533–572. https://doi.org/10.1016/j.jqsrt.2009.02.013, 2009.

Sadrian, M. R., Calvin, W. M., Perrin, A. E., Engelbrecht, J. P., & Moosmüller, H.: Variations in Infrared Complex Refractive Index Spectra of Surface Soils from Global Dust Entrainment Regions. *Atmosphere*, *14*(4), 1–14. https://doi.org/10.3390/atmos14040675, 2023.

Shi, Y., Liu, X., Wu, M., Zhao, X., Ke, Z., & Brown, H.: Relative importance of high-latitude local and long-range-

500   transported dust for Arctic ice-nucleating particles and impacts on Arctic mixed-phase clouds. *Atmospheric Chemistry and Physics*, *22*(4), 2909–2935. https://doi.org/10.5194/acp-22-2909-2022, 2022.

Shonk, J. K. P., Chiu, J. Y. C., Marshak, A., Giles, D. M., Huang, C. H., MacE, G. G., Benson, S., Slutsker, I., & Holben, B. N.: The impact of neglecting ice phase on cloud optical depth retrievals from AERONET cloud mode observations. *Atmospheric Measurement Techniques*, *12*(9), 5087–5099. https://doi.org/10.5194/amt-12-5087-2019, 2019.

505   Shupe, M. D., Turner, D. D., Zwink, A., Thieman, M. M., Mlawer, E. J., & Shippert, T.: Deriving arctic cloud microphysics at Barrow, Alaska: Algorithms, results, and radiative closure. *Journal of Applied Meteorology and Climatology*, *54*(7), 1675–1689. https://doi.org/10.1175/JAMC-D-15-0054.1, 2015.

Stone, R. S., Anderson, G. P., Andrews, E., Dutton, E. G., Shettle, E. P., & Berk, A.: Incursions and radiative impact of Asian dust in northern Alaska. *Geophysical Research Letters*, *34*(14), 1–5. https://doi.org/10.1029/2007GL029878, 2007.

510   Stone, R. S., Sharma, S., Herber, A., Eleftheriadis, K., & Nelson, D. W.: A characterization of Arctic aerosols on the basis of aerosol optical depth and black carbon measurements. *Elementa*, *2*, 1–22. https://doi.org/10.12952/journal.elementa.000027, 2014.

Tobo, Y., Adachi, K., DeMott, P. J., Hill, T. C. J., Hamilton, D. S., Mahowald, N. M., Nagatsuka, N., Ohata, S., Uetake, J., Kondo, Y., & Koike, M.: Glacially sourced dust as a potentially significant source of ice nucleating particles. *Nature*

515   *Geoscience*, *12*(4), 253–258. https://doi.org/10.1038/s41561-019-0314-x, 2019.

Vincent, R. F.: The Effect of Arctic Dust on the Retrieval of Satellite Derived Sea and Ice Surface Temperatures. *Scientific Reports*, *8*(1), 6–15. https://doi.org/10.1038/s41598-018-28024-6, 2018.

Volz, F. E.: Infrared Optical Constants of Ammonium Sulfate, Sahara Dust, Volcanic Pumice, and Flyash. *Applied Optics*, *12*(3), 564. https://doi.org/10.1364/ao.12.000564, 1973.

520   Volz, F. E.: Infrared Refractive Index of Atmospheric Aerosol Substances. Applied Optics, 11(4), 755. https://doi.org/10.1364/ao.11.000755, 1972.

Wald, A. E., Kaufman, Y. J., Tanré, D., & Gao, B. C.: Daytime and nighttime detection of mineral dust over desert using infrared spectral contrast. *Journal of Geophysical Research Atmospheres*, *103*(D24), 32307–32313. https://doi.org/10.1029/98JD01454, 1998.

525   Xi, Y., Xu, C., Downey, A., Stevens, R., Bachelder, J. O., King, J., Hayes, P. L., & Bertram, A. K.: Ice nucleating properties of airborne dust from an actively retreating glacier in Yukon, Canada. *Environmental Science: Atmospheres*, *2*(4), 714–726. https://doi.org/10.1039/d1ea00101a, 2022.

       Yi, L., Li, K. F., Chen, X., & Tung, K. K.: Arctic fog detection using infrared spectral measurements. *Journal of Atmospheric and Oceanic Technology*, *36*(8), 1643–1656. https://doi.org/10.1175/JTECH-D-18-0100.1, 2019.

530   Zamora, L. M., Kahn, R. A., Evangeliou, N., Groot Zwaaftink, C. D., & Huebert, K. B.: Comparisons between the distributions of dust and combustion aerosols in MERRA-2, FLEXPART, and CALIPSO and implications for deposition freezing over wintertime Siberia. *Atmospheric Chemistry and Physics*, *22*(18), 12269–12285. https://doi.org/10.5194/acp-22-12269-2022, 2022.

       Zdanowicz, C., Hall, G., Vaive, J., Amelin, Y., Percival, J., Girard, I., Biscaye, P., & Bory, A.: Asian dustfall in the St.
535 Elias Mountains, Yukon, Canada. Geochimica et Cosmochimica Acta, 70(14), 3493–3507. https://doi.org/10.1016/j.gca.2006.05.005, 2006.

       Zhang, P., Lu, N. meng, Hu, X. qing, & Dong, C. hua.: Identification and physical retrieval of dust storm using three MODIS thermal IR channels. *Global and Planetary Change*, *52*(1–4), 197–206. https://doi.org/10.1016/j.gloplacha.2006.02.014, 2006.

540   Zhao, X., Huang, K., Fu, J. S., & Abdullaev, S. F.: Long-range transport of Asian dust to the Arctic: identification of transport pathways, evolution of aerosol optical properties, and impact assessment on surface albedo changes. *Atmospheric Chemistry and Physics*, *22*(15), 10389–10407. https://doi.org/10.5194/acp-22-10389-2022, 2022.

       Zuidema, P., Baker, B., Han, Y., Intrieri, J., Key, J., Lawson, P., Matrosov, S., Shupe, M., Stone, R., & Uttal, T.: An Arctic springtime mixed-phase cloudy boundary layer observed during SHEBA. Journal of the Atmospheric Sciences, 62(1), 160–
545 176. https://doi.org/10.1175/JAS-3368.1, 2005.